REMARKS

Claims 1-43 are all the claims pending in the Application.

Applicant notes with appreciation that claims 17 and 38 have been indicated as allowable, subject to the 35 U.S.C. § 112 rejections set out below.

Applicant further notes with appreciation that the references considered in parent application Serial No. 09/512,781, as identified in the previously submitted IDS, have been considered.

The drawings have been objected to as not showing every feature of the invention as recited in the claims. Applicant submits herewith a replacement drawing sheet depicting FIG. 3, and a newly submitted drawing sheet depicting new FIGS. 4 and 5. The only change to FIG. 3 is that the optics device shown in this figure has been designated with reference numeral 100. FIG. 4 depicts a monolithic optics device, as recited in, for example, claims 14 and 35. FIG. 5 depicts an monolithic, integrated optics device as recited in, for example, claims 15 and 36. Support for FIGS. 4 and 5 may be found in the specification at, for example, page 7, paragraph [0018], pages 18 and 19, paragraphs [0044] and [0045], and page 20, paragraphs [0048] and [0049].

Applicant declares that the amendments the specification, as well as the replacement and newly submitted drawing sheets submitted herewith contain no new matter. It is believed that these drawing sheets are fully responsive to the objections raised in the Office Action, and Applicant respectfully requests that these objections be withdrawn.

The specification has been objected to because of several informalities. The forgoing amendments are believed to be fully responsive to this objection. Pursuant to the Examiner's request, Applicant has made reasonable efforts to check the specification for

possible errors. The foregoing specification changes have been made. Applicant respectfully requests that this objection also be withdrawn.

Claims 17 and 38 stand rejected under 35 U.S.C. §112, first paragraph, as failing to comply with the enablement requirement. Claims 17 and 38 also stand rejected under 35 U.S.C. §112, second paragraph, as being indefinite. Claim 43 stands rejected under 35 U.S.C. §102(b) as being anticipated by a publication by Ozaktas et al. (JOSA, 1994). Claims 1-16, 18-37, 39- 42 stand rejected under 35 U.S.C. §103(a) as being unpatentable over Ozaktas in view of a number of different references.

Claim Objections

Claim 40 is objected to since it purportedly recites elements of a method without introducing any additional active method steps. It is believed that the foregoing amendment to this claim is fully responsive to the points raised by the Examiner. Accordingly, Applicant respectfully requests that this objection be withdrawn. Applicant notes that the amendment to this claim corrects an obvious error, and the scope of this claim remains unchanged. Note also that claim 39 has been amended for similar reasons, and thus the scope of that claim also remains unchanged.

The Office Action further notes that claims 23 –28, and 30-31 are written in the passive voice, and requests that these claims be rewritten using terminology in the active voice. Applicant respectfully declines the invitation to rewrite these claims for the following reasons.

First, Applicant acknowledges that 35 U.S.C. § 112, second paragraph, requires claims to particularly point out and distinctly claim the invention. The primary purpose of

this requirement of definiteness of claim language is to ensure that the scope of the claims is clear so the public is informed of the boundaries of what constitutes infringement of the patent. MPEP § 2173. A secondary purpose is to provide a clear measure of what an Applicant regards as the invention so that it can be determined whether the claimed invention meets all the criteria for patentability and whether the specification meets the criteria of 35 U.S.C. § 112, first paragraph, with respect to the claimed invention. *Id.*

In claims 23 –28 and 30-31, Applicant has used terminology such as "is determined," "is controlled," and "are accomplished." These limitations are unambiguous, and serve to further limit the invention according to their respective recitations. Applicant recognizes that each of these limitations *could* be rewritten in the active voice, but the relevant patent laws and rules do not *require* the redrafting of these claims. Indeed, a fundamental principle contained in 35 U.S.C. § 112, second paragraph, is that applicants are their own lexicographers. "They can define in the claims what they regard as their invention essentially in whatever terms they choose so long as the terms are not used in ways that are contrary to accepted meanings in the art." MPEP § 2173.01. Accordingly, Applicant respectfully declines the Examiner's invitation to rewrite these claims using the suggested language, and requests that the objection to these claims be withdrawn.

Rejection Under 35 U.S.C. §112, first paragraph

The Examiner has rejected claims 17 and 38 under 35 U.S.C. §112, first paragraph, as failing to comply with the enablement requirement. These claims are directed to a system and method for optically filtering original images comprising a particle beam.

First of all, it is to be understood that the fundamental principles of coherent

Fourier optics also applies to particle beams. As such, the material provided in the specification relating to the filtering of light applies equally to the filtering of particle beams, as is known to one of ordinary skill in the optical imaging art. As set forth below, the specification specifically describes this association between light and particle beams. Moreover, a number of published references addressing electron beam microscopy or electron beam lithography additionally support this position.

One such publication is the modern summary reference by Spense entitled "High-Resolution Electron Microscopy" Oxford 2003. (Attachment A, pages 1-16). Applicant respectfully invites the Examiner to view chapter 2 of the Spense reference entitled "Electron Optics" and chapter 4 entitled "Coherence and Fourier Optics." Sections 4.1 and 4.2 specifically address electrons repeatedly and explicitly in establishing the context for the remaining portions of that chapter. With respect to optical elements for particle beams: section 2.1 discusses electron lenses; figure 2.3 explicitly shows "an electron microscope with two condenser lenses"; table 2.1 lists focal lengths of such lenses; section 2.5 discusses electron projector lenses; section 2.5 discusses electron objective lenses; and figure 2.10 compares physics of objective and projector electron lenses.

Spatial filtering, via apertures such as grids, gratings, and pin holes, is also known for coherent radiation. This topic is addressed in a publication by Chang et al. entitled "Spatial Coherence Characterization of Undulator Radiation" (http://www-als.lbl.gov/als/compendium/AbstractManager/uploads/99137.pdf) (Attachment A, pages 17-19). Chang discusses filtering by magnetic or electrostatic fields, diffraction, and of course transmission through spatially variant materials which is a major focus of transmission electron microscopy (for example, see the basic transmission electron

microscope reference located at http://www.unl.edu/CMRAcfem/temoptic.htm) (Attachment A, pages 20-21).

Notwithstanding the known association between coherent Fourier optics and particle beams, the present specification states that optical filtering according to embodiments of the invention apply to "conventional lens-based optical image processing systems as well as to systems with other types of elements obeying Fractional Fourier optical models and as well as to widely ranging environments such as ... particle beam systems ... ." (emphasis added) (See Specification, page 1, para. [0002]; see also page 7, para. [0018]; page 20 para. [0048]).

The specification clearly enables one of ordinary skill to practice the claimed invention with regard to the filtering of light. Applicant has also demonstrated that it is well known that the principles of coherent Fourier optics also applies to particle beams. Furthermore, Applicant has identified various exemplary portions of the specification which state that the disclosed optical filtering systems and methods relate to "particle beam systems." For these reasons, the present disclosure provides more than the requisite teaching to enable one of ordinary skill to make and use the invention recited in claims 17 and 38, which each recite a particle beam.

Rejection Under 35 U.S.C. §112, second paragraph

The Examiner has further rejected claims 17 and 38 under 35 U.S.C. §112, second paragraph, as being indefinite.

It seems that the basis for the rejection of these claims hinges on the purported lack of disclosure of particle beams as associated with original images. However,

Applicant has demonstrated above in the comments to the rejection under 35 U.S.C. §112, first paragraph, that the principles of coherent Fourier optics also applies to particle beams. Applicant has also shown that the instant specification specifically states that embodiments of the invention apply to conventional lens-based optical image processing systems as well as to particle beam systems. (See Specification, page 1, para. [0002]; see also page 7, para. [0018]; page 20 para. [0048]). Consequently, the specification not only describes embodiments in which the original image comprises light (claim 16 and 37) but also describes embodiments in which the original image comprises a particle beam (claims 17 and 38).

Claims 17 and 38 clearly and distinctly claim the aspect in which the original image comprise a particle beam and are therefore not indefinite under 35 U.S.C. §112, second paragraph, as asserted in the Office Action. For the foregoing reasons, Applicant requests that the various rejections to claims 17 and 38 under 35 U.S.C. § 112, first and second paragraph, be withdrawn.

Rejection Under 35 U.S.C. §102(b) as being Anticipated by Ozaktas

The Examiner rejects claim 43 under 35 U.S.C. §102(b) as being anticipated by a publication by Ozaktas. Independent claim 43 is directed to a method which includes selecting a positive-definite optical transfer function element based upon which non-positive-definite transfer function is to be applied to an image.

Applicant's review of Ozaktas reveals a discussion relating to optical filtering using noise reduction. For example, figures 3-5 on page 554 of the Ozaktas reference depict various filtering schemes that have been selected to achieve some desired noise

separation. Ozaktas further describes the selection of binary on-off amplitude masks based on noise separation on a particular domain (Ozaktas, page 554, right column). Ozaktas specifically mentions that noise separation can be accomplished by three consecutive filtering operations using three different types of amplitude masks (Ozaktas, page 554, right column, first partial paragraph).

Applicant assumes *arguendo* that the binary amplitude masks of Ozaktas, as asserted in the Office Action, teach a positive-definite optical transfer element as recited by claim 43. Ozaktas would therefore provide, at best, the selecting of a positive-definite optical transfer function element (binary amplitude mask) based upon noise separation that is desired in a particular domain. More importantly, this reference does not even mention the selection of a transfer element for any other reason other than to filter noise. Accordingly, Ozaktas cannot teach or suggest the selecting of a transfer function element based upon which non-positive-definite transfer function is to be applied to an image, as specifically recited in claim 43. In view of the foregoing, Ozaktas fails to teach or suggest at least one feature recited in independent claim 43 and therefore this claim is believed to be patentable.

Rejections Under 35 U.S.C. §103(a)

The Examiner next rejects claims 1-16, 18-37, 39-42 under 35 U.S.C. §103(a) as being unpatentable over Ozaktas in view of an number of different references.

Independent claim 1 is directed to a system having a positive-definite optical transfer function element having a plurality of non-zero transmission amplitude values.

In the Office Action, Ozaktas is characterized as disclosing an amplitude mask

positioned within a region that is outside a Fourier transform plane (Office Action, page 7, first partial paragraph). Applicant's review of Ozaktas reveals a discussion on the use of "binary on-off amplitude mask filters" (Ozaktas, page 554, right column, first full paragraph). The amplitude mask filters described by Ozaktas are limited to only two possible amplitude values; specifically, on or off. Simply put, the binary filters of Ozaktas either transmit or block a received signal. Furthermore, Ozaktas lacks any disclosure relating to any other type of filtering schemes and as such, lacks any teaching or suggestion relating to a transfer function element having a <u>plurality of</u> non-zero transmission amplitude values.

Applicant assumes for the sake of argument that the binary amplitude masks of Ozaktas teach a positive-definite optical transfer element as recited by claim 1. Ozaktas would therefore provide, at best, a transfer function element (binary amplitude mask) that has only two possible amplitude values. Although the Ozaktas transfer function element has two possible values, <u>only one</u> of these values is non-zero. As such, the transfer function element of Ozaktas only provides <u>a single</u> non-zero transmission amplitude. The binary masks of Ozaktas are incapable of providing more than one non-zero transmission amplitude and thus this reference cannot teach a transfer function element having <u>a plurality</u> of non-zero transmission amplitude values, as recited by claim 1.

Applicant further notes that none of the cited references teach or suggest a transfer function element having <u>a plurality</u> of non-zero transmission amplitude values and therefore none of these reference can remedy the deficiencies of Ozaktas. Accordingly, even if one skilled in the art were to combine the teachings of these references in the manner asserted, the resulting system would not teach or suggest all of

the recited claim elements. For these reasons, claim 1 is also believed to be patentable and dependent claims 2-16, and 18-21 would also be patentable at least by virtue of their dependence upon claim 1.

Independent claim 22 is directed to a method which includes selecting a positive-definite optical transfer function element based upon <u>which non-positive-definite transfer function</u> is to be applied to the original image. Applicant has demonstrated above that Ozaktas does not teach or suggest this particular feature. Applicant further notes that none of the cited references supply any of the stated deficiencies of Ozaktas. Therefore, for the reasons presented above, even if one skilled in the art were to combine the teachings of these references in the manner asserted, the process disclosed by the various references would not teach or suggest all of the recited claim elements of claim 22. Based on the foregoing, claim 22 is also believed to be patentable and dependent claims 23-33, 35-37, and 39-42 would also be patentable at least by virtue of their dependence upon claim 22.

In addition, Applicant has reviewed the various cited but not applied references identified on page 16 of the Office Action. They are interesting and appear to be generally related technology, but there is nothing of sufficient relevance to require detailed discussion.

CONCLUSION

Applicant believes that the Examiner's rejections have been overcome and submits that the subject application is in condition for allowance. Should any issues remain unresolved, the Examiner is invited to telephone the undersigned attorney.

The Commissioner is hereby authorized to charge any fees that arise in

connection with this filing which are not covered by the money enclosed, or credit any overpayment, to Deposit Account No. 02-0460.

Respectfully submitted,

LESTER F. LUDWIG

By: Jeffrey J. Lotspeich
Attorney for Applicant
Registration No. 45,737

Dated: October 5, 2004

THE MAXHAM FIRM
750 'B' STREET, SUITE 3100
SAN DIEGO, CALIFORNIA 92101
TELEPHONE: (619) 233-9004
FACSIMILE: (619) 544-1246

ATTACHMENT A
Ser. No.: 10/656,342
Page 1

MONOGRAPHS ON THE PHYSICS AND CHEMISTRY OF MATERIALS

Theory of dielectrics M. Frohlich
Strong solids (Third edition) A. Kelly and N. H. Macmillan
Optical spectroscopy of inorganic solids B. Henderson and G. F. Imbusch
Quantum theory of collective phenomena G. L. Sewell
Principles of dielectrics B. K. P. Scaife
Surface analytical techniques J. C. Rivière
Basic theory of surface states Sydney G. Davison and Maria Steslicka
Acoustic microscopy Andrew Briggs
Light scattering: principles and development W. Brown
Quasicrystals: a primer (Second edition) C. Janot
Interfaces in crystalline materials A. P. Sutton and R. W. Balluffi
Atom probe field ion microscopy M. K. Miller, A. Cerezo, M. G. Hetherington, and G. D. W. Smith
Rare-earth iron permanent magnets J. M. D. Coey
Statistical physics of fracture and breakdown in disordered systems B. K. Chakrabarti and L. G. Benguigui
Electronic processes in organic crystals and polymers (Second edition) M. Pope and C. E. Swenberg
NMR imaging of materials B. Blümich
Statistical mechanics of solids L. A. Girifalco
Experimental techniques in low-temperature physics (Fourth edition) G. K. White and P. J. Meeson
High-resolution electron microscopy (Third edition) J. C. H. Spence

HIGH-RESOLUTION ELECTRON MICROSCOPY

THIRD EDITION

JOHN C. H. SPENCE

Department of Physics and Astronomy
Arizona State University

OXFORD
UNIVERSITY PRESS

OXFORD
UNIVERSITY PRESS

Great Clarendon Street, Oxford OX2 6DP

Oxford University Press is a department of the University of Oxford.
It furthers the University's objective of excellence in research, scholarship,
and education by publishing worldwide in

Oxford New York

Auckland Bangkok Buenos Aires Cape Town Chennai
Dar es Salaam Delhi Hong Kong Istanbul Karachi Kolkata
Kuala Lumpur Madrid Melbourne Mexico City Mumbai Nairobi
São Paulo Shanghai Taipei Tokyo Toronto

Oxford is a registered trade mark of Oxford University Press
in the UK and in certain other countries

Published in the United States
by Oxford University Press Inc., New York

First edition 1980
Second edition 1988
Third edition 2003
Previously editions were entitled *Experimental high-resolution electron microscopy*

A catalogue record for this title is available from the British Library

Library of Congress Cataloging in Publication Data

Spence, John C. H.
High-resolution electron microscopy / John C. H. Spence—3rd ed.
(Monographs on the physics and chemistry of materials)
Rev. ed. of: Experimental high-resolution electron microscopy. 2nd ed. 1988.
Includes bibliographical references.
1. Transmission electron microscopy. I. Spence, John C. H. Experimental
high-resolution electron microscopy. II. Title III. Series.
QH212.T7 S68 2003 502'.8'25—dc21 2002030302

ISBN 0 19 850915 4

10 9 8 7 6 5 4 3 2 1

Typeset by Newgen Imaging Systems (P) Ltd., Chennai, India
Printed in Great Britain
on acid-free paper by
Biddles Ltd., Guildford & King's Lynn

To
Vernon, Penny and Andrew

eqn (6.16). A through-focus series about the minimum contrast focus in steps of, say 20 nm, will show the characteristic change from a dark over-focus Fresnel fringe around an atom cluster to a bright fringe in the under-focus images.

7. Digital diffractograms of the images should be obtained as described in Section 10.7. The measured diameter of the rings seen in these can be used with the simple computer program given in Appendix 1 to find the focus setting for each micrograph and the microscope's spherical aberration constant. More immediately, these optical diffraction patterns reveal at a glance the presence of astigmatism or specimen movement during the exposure (drift—see Section 10.7). This immediate 'feedback' is essential for a microscopist learning the skills of astigmatism correction and focusing. With practice the microscopist will become adept at finding the minimum-contrast condition, correcting astigmatism, and resetting the focus control a fixed number of 'clicks' toward the under-focus side to obtain images of highest contrast and resolution.

References

Agar, A. W., Alderson, R. H., and Chescoe, D. (1974). Principles and practice of electron microscope operation. In *Practical Methods in Electron Microscopy* (ed. A. M. Glauert). North-Holland, Amsterdam.

Alderson, R. H. (1974). The design of the electron microscope laboratory. In *Practical Methods in Electron Microscopy* (ed. A. M. Glauert). North-Holland, Amsterdam.

Bennett, A. H., Jupnik, H., Osterberg, H., and Richards, O. W. (1951). *Phase Microscopy. Principles and Applications*. Wiley, New York.

Cosslett, V. E. (1958). Quantitative aspects of electron staining. *J. R. Microsc. Soc.* **78**, 18.

Downing, K. H. and Siegel, B. M. (1973). Phase shift determination in single-sideband holography. *Optik* **38**, 21.

Goodman, J. W. (1968). *Introduction to Fourier Optics*. McGraw-Hill, New York.

Lipson, S. G. and Lipson, H. (1969). *Optical Physics*. Cambridge University Press, London.

Spence, J. C. H. (1974). Complex image determination in the electron microscope. *Opt. Acta* **21**, 835.

Unwin, N. (1971). Phase contrast and interference microscopy with the electron microscope. *Phil. Trans. R. Soc., Lond.* **B261**, 95.

2

ELECTRON OPTICS

An elementary knowledge of electron optics is important for the intelligent use of an electron microscope, particularly at high resolution. This chapter is intended to give the simplest account of electron optics that will expose the important physical properties of magnetic electron lenses, such as image rotation, aberrations, minimum focal length, and the distinction between projector and objective modes. In high-resolution work it is common practice to experiment with changes in specimen position, the effects of which can be understood from the discussion of Section 2.7. It is also sometimes convenient to increase the overall magnification available on an older machine—the effect of the projector lens pole-piece dimensions on magnification is also mentioned. Some calculations of lens characteristics used for lens design are also given, showing the way in which lens aberrations, of prime importance at high resolution, depend on the lens excitation and geometry. Since the emphasis is on the practical aspects of the behaviour of real lenses, I do not discuss the elegant and considerable contribution of early workers using simple algebraic approximations for the lens field. These workers' investigations, such as those of Lenz, Glaser, Grivet, and Ramberg, can be traced through the electron optics texts included in the references for this chapter. Useful introductory accounts of electron optics can be found in the books by Hall (1966) and Hawkes (1972). Grivet (1965) is a useful general text on electron optics for the solution of practical electron-optical problems. Modern lens designs are guided by a great deal of experience, together with computed solutions of the Laplace equation (Septier 1967) for a review of methods for doing this) and subsequent numerical solution of the ray equation (see, e.g. Mulvey and Wallington (1972) or Kamminga *et al.* (1968/9)). The accurate measurement of electron-optical parameters such as the spherical aberration and chromatic aberration constants, which has become increasingly important with developments in image analysis at high resolution, is discussed

ATTACHMENT A
Ser. No.: 10/656,342
Page 4

in Chapter 10. Developments in superconducting electron optics are described in Dietrich (1977).

2.1 The electron wavelength and relativity

Rather than solve the Schrödinger equation for the electron microscope as a whole, it is simpler to separate the three problems of beam—specimen interactions, magnetic lens action, and fast electron sources. The first problem is a many-body problem solved by optical-potential methods, while the second has traditionally been treated classically. A wavelength is assigned to the fast electron as follows.

The principle of conservation of energy applied to an electron of charge $-e$ traversing a region in which the potential varies from 0 to V_0 gives

$$eV_0 = p^2/2m = h^2/2m\lambda^2 \tag{2.1}$$

where p is the electron momentum and h is Planck's constant. Thus,

$$\lambda = \frac{h}{\sqrt{2meV_0}} \tag{2.2}$$

where the de Broglie relation $p = mv = h/\lambda$ has been used. An electron leaves the filament with high potential energy and thermal kinetic energy, and arrives at the anode with no potential energy and high kinetic energy. The zero of potential energy is taken at ground potential. If λ is in nanometres and V_0 in volts, then

$$\lambda = 1.22639/\sqrt{V_0} \tag{2.3}$$

At higher energies the relativistic variation of electron mass must be considered. Neglect of this leads to a 5 per cent error in λ at 100 kV. The relativistically corrected mass is

$$m = m_0/(1 - v^2/c^2)^{1/2}$$

and the equation corresponding to (eqn 2.1) is

$$eV_0 = (m - m_0)c^2$$

with m_0 the electron rest mass and c is the velocity of light. These equations may be combined to give an expression for the electron momentum mv. Used in the de Broglie

relation, this gives the corrected electron wavelength as

$$\lambda = h/(2m_0eV_r)^{1/2} \tag{2.4}$$

where

$$V_r = V_0 - \left(\frac{e}{2m_0c^2}\right)V_0^2$$

is the 'relativistic accelerating voltage', introduced as a convenience. For computer calculations discussed in later chapters the value of λ may be taken as

$$\lambda = 1.22639/(V_0 + 0.97845 \times 10^{-6}V_0^2)^{1/2} \tag{2.5}$$

with V_0 the microscope accelerating voltage in volts and λ in nanometres.

The relativistic correction is important for high-voltage electron microscopy (HVEM). If V_0 is expressed in MeV, a good approximation is $V_r = V_0 + V_0^2$, so that $V_r = 6$ MeV for a 2 MeV microscope. The largest instruments currently available operate at 3 MeV. The formal justification for these definitions of a relativistically corrected electron mass and wavelength must be based on the Dirac equation, as first pointed out by A. Howie and K. Fujiwara (see Section 5.7).

A method for measuring the relativistically corrected electron wavelength directly from a diffraction pattern is discussed in Chapter 10. This method requires only a knowledge of a crystal structure and does not require the microscope accelerating voltage or camera length to be known.

The positive electrostatic potential ϕ_0 inside the microscope specimen further accelerates the incident fast electron, resulting in a small reduction in wavelength inside the specimen (Fig. 2.1). Ignoring the periodic variation of specimen potential, which gives rise to diffraction and the dispersion surface construction, the mean value of this inner potential is given by v_0, the zero-order Fourier coefficient of potential (see Section 5.3.2). A typical value of u_0 is 10 V. The refractive index of a material for electrons is then given by the ratio of wavelength λ in vacuum to that inside the specimen λ'. Applying the principle of conservation of energy with careful regard to sign gives

$$n = \frac{\lambda}{\lambda'} = \left(\frac{1.23}{\sqrt{V_0}}\right)\left(\frac{\sqrt{V_0 + \phi_0}}{1.23}\right) \approx 1 + \frac{\phi_0}{2V_0}$$

The phase shift of a fast electron passing through a specimen of thickness t with respect to that of the vacuum wave is then

$$\theta = 2\pi(n-1)t/\lambda = \pi\phi_0 t/\lambda V_0 = \sigma\phi_0 t$$

as suggested in Fig. 2.2. Here $\sigma = \pi/\lambda V_0 = 2\pi me\lambda/h$. If the approximation is then made that the exit face wavefunction can be found by computing its phase along a single optical path such as AB in Fig. 2.2, the product $\phi_0 t$ can be replaced by the specimen potential function projected in the direction of the incident beam (see Section 3.4). The neglected contributions from paths such as CA can be included using the Feynman path-integral method as discussed in Jap and Glaeser (1978).

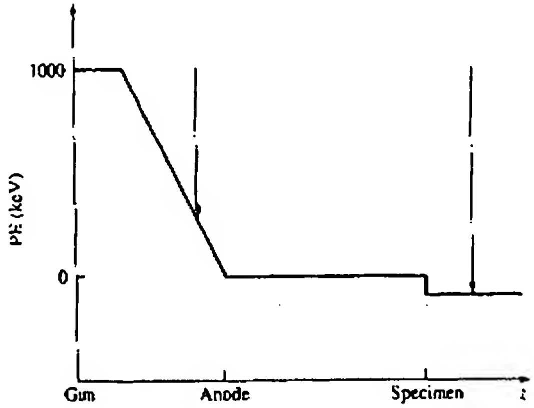

Fig. 2.1 Simplified potential energy diagram for an electron microscope. The length of the vertical arrow is proportional to the kinetic energy of the fast electron, and inversely proportional to the square of its wavelength. The sum of the electron's potential energy (represented by the height of the graph) and its kinetic energy is constant. Electrons leave the filament with low kinetic energy and high potential energy (supplied by the high-voltage set) and exchange this for kinetic energy on their way to the anode, which is at ground potential. As with a ball rolling down a hill, they are further accelerated as they 'fall in' to the specimen. Approximate distance down the microscope column is represented on the abscissa and the potential step at the specimen has been exaggerated.

2.2 Simple lens properties

Modern electron microscopes use four or five imaging lenses, of variable focal length, below the specimen with the position of the object and final viewing screen fixed for the purposes of focusing. At the high magnifications usually used for high-resolution work, the lens currents (which determine the focal lengths) of lenses L2, L3, and L4 are used to control the magnification as shown in Fig. 2.3 and Table 2.1. For a fixed magnification setting, focusing is achieved by adjusting the strength of the objective lens L1 until the fixed plane P1 is conjugate to the exit face of the specimen. Some of the properties of these lenses can be understood from the equations describing ideal lens behaviour given below, which also provide results used in later chapters.

The study of electron optics seeks to determine the conditions under which the electron wavefield passing through an electron lens satisfies the requirements for perfect image formation. For comparison purposes, it is convenient to set up the model of the ideal lens. The ideal lens is a mathematical abstraction which provides perfect imaging given by a projective transformation between the object and image space. The constants appearing in this transformation specify the positions of the cardinal planes of the lens. The six important cardinal planes are the two focus planes, the two principal planes, and the two nodal planes as shown in Fig. 2.4. For magnetic lenses the nodal planes coincide with the principal planes. The points where the axis crosses the nodal planes are called nodal points, N1 and N2. Principal planes

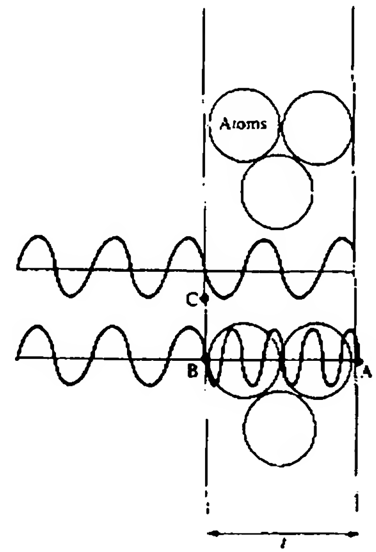

Fig. 2.2 The electron wave illustrated in two cases passing through a specimen. The wave passing through the centre of an atom (where the potential is high) has its wavelength reduced and so suffers a phase advance relative to the wave passing between the atoms which experiences little change in its wavelength. The assumption of this simplified model used in the phase grating approximation is that the amplitude at A can be calculated along the optical path AB with no contribution at A from a point such as C. For thick specimens this approximation is unsatisfactory.

are planes of unit lateral magnification, while nodal planes are planes of unit angular magnification. For an axially symmetric lens, the projective transformation for perfect imaging simplifies to

$$\frac{y_i}{y_0} = \frac{f_i}{x_0} = \frac{x_i}{f_0} \tag{2.6}$$

where the symbols are as defined in Fig. 2.4. The second of these equations is Newton's lens equation. Figure 2.4 provides a convenient graphical construction for eqn (2.6). Here F1 and F2 are known as the object and image focus respectively with H1 and H2 the object and image principal planes. The determination of the positions of these planes is the key problem of electron optics—once they are known the rules for graphical construction of figures satisfying eqn (2.6) can be used to find the image of an arbitrary object. The rule for a construction which gives the conjugate image point of a known object point P is:

1. Draw a ray through P and F1, intersecting H1 at Q. Through Q draw a ray YQ parallel to the axis extending into both object and image spaces.
2. Draw a ray parallel to the axis through P to intersect H2. From this intersection draw a ray through F2 to intersect the ray YQ at P′. P′ is the image of P.

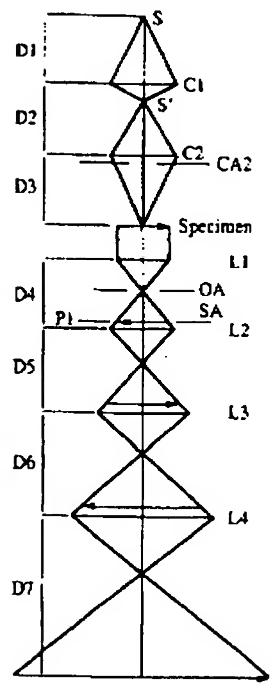

Fig. 2.3 Ray diagram for an electron microscope with two condenser lenses, C1 and C2 and four imaging lenses, L1, L2, L3, and L4, operating at high magnification. A typical set of dimensions for $D1$ to $D7$ is given in Table 2.1, together with the possible range of focal lengths. These values may be used for examples throughout this book. Here OA is the objective aperture, P1 is a fixed plane, and SA is the selected area aperture.

Table 2.1 Electron-optical data for a typical electron microscope (see Fig. 2.3)

Distances between lens centres (approximate) (mm)	Focal length range (m)
$D1 = 143.6$	$1.65 < f(\mathrm{C1}) < 19$
$D2 = 94.3$	$30 < f(\mathrm{C2}) < 1060$
$D3 = 251.4$	$15.4 < f(\mathrm{L2}) < 281$
$D4 = 215.5$	$3.1 < f(\mathrm{L3}) < 99.5$
$D5 = 44.9$	$2.06 < f(\mathrm{L4}) < 16.4$
$D6 = 73.6$	
$D7 = 345.6$	

For magnifications greater than 100 000 the magnification is controlled adjusting the focal length of L3 with $f(\mathrm{L2}) = 15.4$ mm fixed and $f(\mathrm{L4}) = 2.1$ mm fixed. The focal length of L3 is set as follows: $f(\mathrm{L3}) = 9.8, 7.0, 5.0, 3.1$ mm for $M = 150, 200, 400, 750$K, respectively.

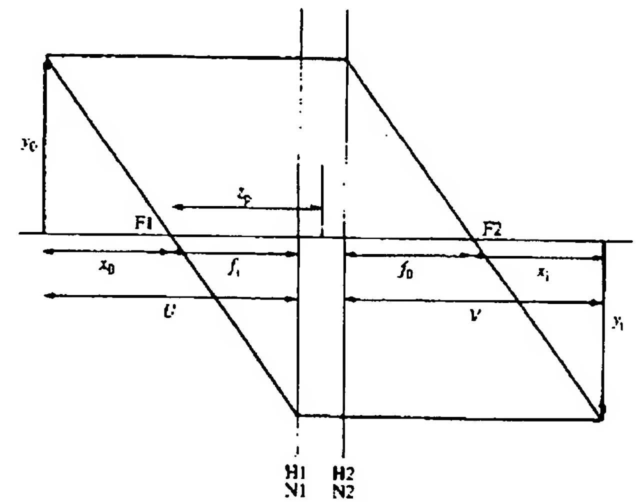

Fig. 2.4 The thick lens. The nodal planes (N1, N2), principal planes (H1, H2), and focal planes (F1, F2) are shown together with the lens focal lengths (f_i, f_0) and the object focal distance z_p. For a magnetic electron lens the principal planes are crossed.

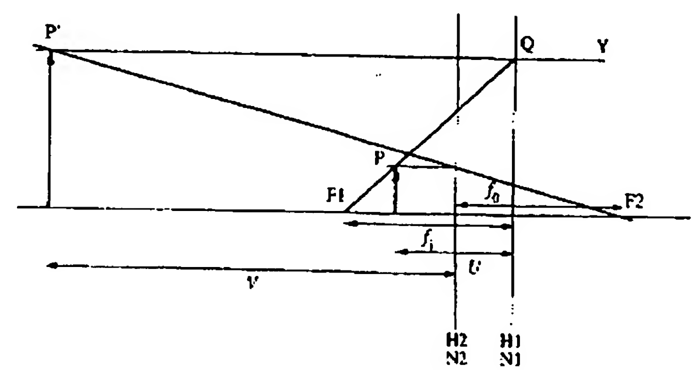

Fig. 2.5 Ray diagram for the objective lens of a microscope operating at moderate magnification. The image is virtual and the principal planes are crossed. Object and image focal lengths are equal for magnetic lenses. A typical value for f_2 is 2 mm, and the magnification $M = V/U$ may be about 20.

As an example of this construction, Fig. 2.5 shows these rules applied to the objective lens of a modern electron microscope operating at moderate magnification (about 40 000). Note that the image formed by the objective lens is virtual, and that the principal planes are crossed, as they are for all magnetic electron lenses. The use of this mode on a four-lens instrument has advantages for biological specimens

ATTACHMENT A
Ser. No.: 10/656,342
Page 7

where radiation damage must be minimized. At this moderate magnification lens L3 is switched off. At high magnification all lenses are used. Modern lens designers use the methods of matrix optics; an elementary introduction to these techniques can be found in Nussbaum (1968).

The simple thin-lens formula can still be used if the object and image distances U and V are measured from the lens principal planes H1 and H2.

Equation (2.6) becomes

$$\frac{f_i}{U} + \frac{f_0}{V} = 1$$

If the refractive indices in the object and image space are equal, as they are for magnetic electron lenses, then

$$f_i = f_0 = f \tag{2.7}$$

and so

$$\frac{1}{U} + \frac{1}{V} = \frac{1}{f} \tag{2.8}$$

A construction can also be given to enable the continuation of a ray segment in the image space to be found if it is known in the object space. Note that a ray from P arriving at N1 at an arbitrary angle leaves N2 at the same angle. For a thin lens the principal planes coincide, so this is the ray through the lens origin. Equation (2.8) is quite general if the following sign convention is obeyed: U is positive (negative) when the object is to the left (right) of H1, V is positive (negative) when the image is to the right (left) of H2. Both focal lengths are positive for a convergent lens, and all magnetic lenses are convergent for electrons and positrons. From eqn (2.8) and the definition of magnification (eqn 2.9) three cases emerge:

1. $U < f$. Image is virtual, erect, and magnified.
2. $f < U < 2f$. Image is real, inverted, and magnified.
3. $U > 2f$. Image is real, inverted, and reduced.

Some additional terms, commonly used in electron optics, are defined below.

1. The lateral magnification M is given by

$$M = \frac{y_i}{y_0} = -\frac{V}{U} \tag{2.9}$$

Using eqn (2.8) we have

$$M - 1 = -\frac{V}{f} \tag{2.10}$$

so that if V is fixed and the magnification is large, as it is for the objective lens of an electron microscope, the magnification is inversely proportional to the objective

lens focal length. For high magnification, U must be slightly greater than f—both are about a millimetre for a high-resolution objective lens.

2. The angular magnification m is, for small angles,

$$m = \frac{\tan\theta_i}{\tan\theta_0} \approx \frac{\theta_i}{\theta_0} = \left|\frac{1}{M}\right| \tag{2.11a}$$

as shown in Fig. 2.6.

3. The entrance and exit pupil of an optical system are important in limiting its resolution and light-gathering power. These concepts also simplify the analysis of complex optical systems. The entrance pupil is defined as the image of that aperture, formed by the optical system which precedes it, which subtends the smallest angle at the object. The image of the entrance pupil formed by the whole system is known as the exit pupil. The 'aperture stop' is the physical aperture whose image forms the entrance pupil, as shown in Fig. 2.7.

4. The Gaussian reference sphere for an image point P is defined as the sphere, centred on P, which passes through the intersection of the optic axis with the exit pupil (see Fig. 2.7). For an unaberrated optical system, the surface of constant phase for a Huygens spherical wavelet converging toward P coincides with this reference sphere. The deviation of the wavefront from the Gaussian reference sphere specifies the aberrations of the system (see Section 3.3), while the diffraction limit is imposed by the finite size of the exit pupil, or, equivalently, the entrance pupil. This is discussed further in Chapter 3.

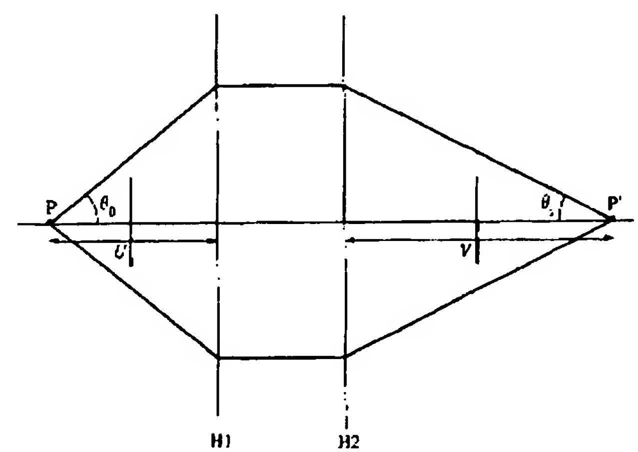

Fig. 2.6 Angular magnification. The image P' of a point P is shown together with the angles which a ray makes with these points.

Sep-21-04 04:27P Lester Ludwig / NRI

ATTACHMENT A
Ser. No.: 10/656,342
Page 8

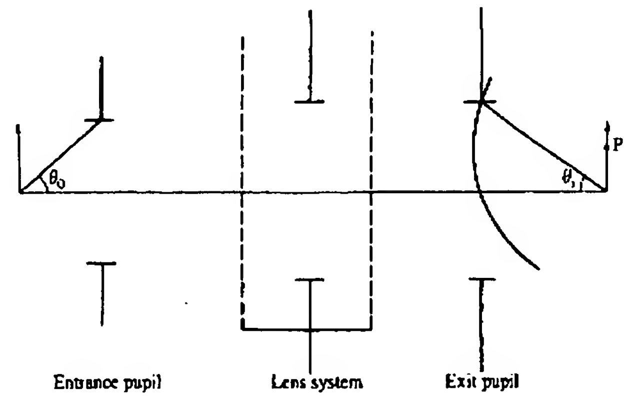

Fig. 2.7 The entrance and exit pupils of an optic system. A complicated optical system consisting of many lenses can be treated as a 'black box' and specified by its entrance and exit pupils and a complex transfer function. A Huygens spherical wavefront is shown converging to an image point P.

5. The longitudinal magnification, M_z, can be used to relate depth of field to depth of focus (see below). Differentiation of eqn (2.8) gives

$$\frac{\Delta V}{\Delta U} = -M^2 = M_z \tag{2.11b}$$

Thus an object displacement ΔU causes a displacement ΔV of conjugate image planes given by this equation. For example the image planes conjugate to the upper and lower surfaces of an atom 0.3 nm 'thick' are separated by 3 m if the lateral magnification M is 100 000.

6. Incoherent imaging theory gives the depth of field or range of focus values (referred to the object plane) over which an object point can be considered 'in focus' as $2d/\theta$, where θ is the objective aperture semi-angle and d is the microscope resolution. This result cannot, however, be accurately applied to the coherent high-resolution imaging of phase objects (see Section 3.4).

The methods used by lens designers to determine the position of the cardinal planes of electron lenses are discussed in the next sections. From Fig. 2.4 it is seen that the axis crossing of a ray entering (leaving) parallel to the axis defines the image (object) focus. In electron optics the trajectory of an electron entering the lens field parallel to the axis can similarly be used to find the lens focus once the equation of motion for the electron can be solved for a particular magnetic field distribution. Real electron trajectories follow smooth curves within the lens magnetic field. In order to use the ideal lens model it may be necessary to use the virtual extensions of a ray from a point well outside the influence of the field to define the lens focus.

2.3 The paraxial ray equation

The focusing action of an axially symmetric magnetic field can be understood as follows. Figure 2.8 shows a simplified diagram of an electron lens, including a typical line of magnetic flux. The actual arrangement used for one instrument in the important region of the lens pole-pieces is shown in Fig. 2.9. The dimensions of the pole-piece are S, R_1, and R_2 as shown in Fig. 2.8. The magnetic field B is confined to the pole-piece gap, where an electron of charge $-e$ and velocity v experience a force

$$F = -ev \times B = m\frac{d^2r}{dt^2} \tag{2.12}$$

The direction of F is given by the left-hand rule (current flow opposite to electron flow), which from Fig. 2.8 is seen to be into the page as the electron enters the field on the left (assuming the upper pole-piece is a North pole). An electron entering on the right side experiences a force out of the page. These forces result in a helical rotation of the electron trajectory. The rotational velocity component r_θ imparted interacts with the z component of the field $B_z(r)$ to produce a force towards the axis, again given by the left-hand rule. This force is responsible for the focusing action of the lens.

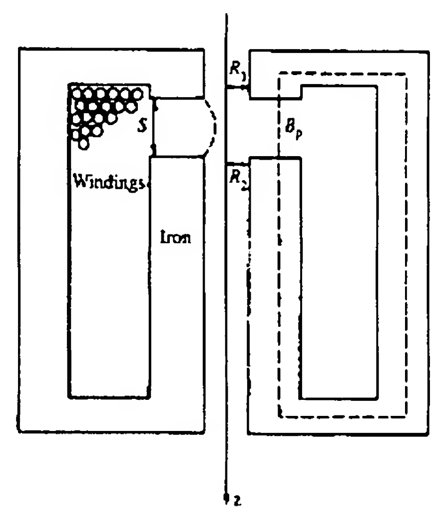

Fig. 2.8 Simplified diagram of a magnetic electron lens. The dimensions of the pole-piece are indicated and the path taken for Ampère's law is shown as a broken line. Also broken is shown a line of magnetic flux which gives a qualitative indication of the focusing action of the lens (see text). The field strength in the gap far from the optic axis is B_p. In practice the windings are water cooled and the pole-piece is removable.

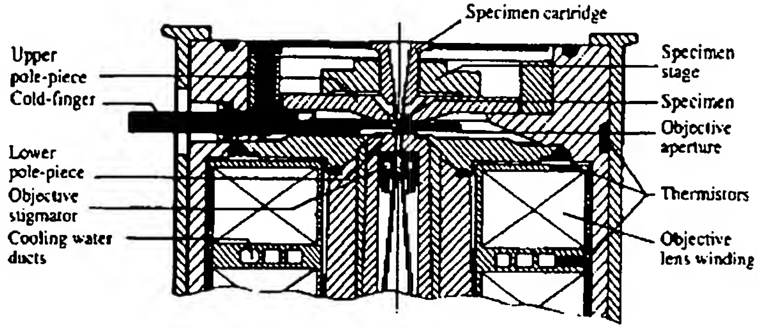

Fig. 2.9 Detail of an actual high-resolution pole-piece. The upper pole-piece bore diameter $2R_1$ is 9 mm, the lower bore diameter $2R_2$ is 3 mm, and the gap S is 5 mm in this commercial design. (See Fig. 2.8 for the definitions of R_1, R_2, and S.)

Using certain approximations described in most optics texts, eqn (2.12) can be simplified for meridional rays in a cylindrical coordinate system. These are rays in a plane containing the axis before reaching the lens. The simplifications include the neglect of terms which would lead to imperfect imaging (lens aberrations). The paraxial ray equation which results contains only the z component of the magnetic field evaluated on the optic axis $B_z(z)$. This is

$$\frac{d^2r}{dz^2} + \frac{e}{8mV_r}B_z^2(z)r = 0 \qquad (2.13)$$

where r is the radial distance of an electron from the optic axis and V_r is the relativistically corrected accelerating voltage. Once the field $B_z(z)$ on the axis is known, computed solutions of eqn (2.13) can be used to trace the trajectory of an electron entering the field. For a symmetrical lens, a ray entering parallel to the axis will define all the electron lens parameters discussed in later sections. Note that the approximation has been made that the z component of the field does not depend on r.

Equation (2.13) is a linear differential equation of second order with two linearly independent solutions. It can be shown that these solutions describe rays which satisfy the conditions for perfect lens action. Using a computer one can also solve eqn (2.12) to find the electron trajectories for a particular magnetic field. By comparing these true electron trajectories with the idealized trajectories satisfying eqn (2.13) (and producing perfect imaging) it is possible to determine the aberrations of a magnetic lens. Alternatively, it is possible to use simple expressions for the various aberration coefficients which are given as functions of the solution to eqn (2.13) (see Section 2.8.1).

Similarly, the helical rotation of meridional rays can be found. The rotation of this plane is given by

$$\theta_0 = \left(\frac{e}{8mV_r}\right)^{1/2} \int_{z_1}^{z_2} B_z(z)\,dz. \qquad (2.14)$$

Rays entering the lens in a given meridional plane remain in that plane which rotates through θ_0 as the rays traverse the lens field. Note that the total image rotation is $(180 + \theta_0)$ degrees on account of the image inversion (M is negative).

It can be seen that the lens shown in Fig. 2.8 is very inefficient since most of the power dissipated supports a field in the z direction which produces no force on the electron entering parallel to the axis. Aberration correctors use the far more efficient hexapoles and Quadrupoles.

2.4 The constant-field approximation

A review of computing methods used in the solution of eqn (2.13) is given in Mulvey and Wallington (1972). However, eqn (2.13) is easily solved if the z dependence of the field can be neglected. It then resembles the differential equation for harmonic motion. The accuracy of this 'constant field' approximation has been investigated by Dugas *et al.* (1961), who found it to give good agreement with experiment for the focal lengths of projector lenses at moderate and weak excitation. It is included here for the physical insight it allows into magnetic lens action and to clarify the definition of the lens focal length. Since the expression for C_s (eqn 2.32) involves derivatives of the field, we cannot expect to understand the influence of aberrations using such a crude model.

If the origin of coordinates is taken on a plane midway between the pole-piece gap (length S), then a field constant in the z direction is given by

$$\begin{aligned} B_z(z) &= B_p \quad \text{for } -S/2 \leqslant z \leqslant S/2 \\ &= 0 \quad \text{elsewhere} \end{aligned} \qquad (2.15)$$

Equation (2.13) becomes

$$\frac{d^2r}{dz^2} + k^2r = 0 \qquad (2.16)$$

with

$$k^2 = \left(\frac{e}{8m_0V_r}\right)B_p^2 \qquad (2.17)$$

that is,

$$k = 1.4827 \times 10^5 B_p / V_r^{1/2}$$

with B_p in teslas and V_r in volts. The solution to eqn (2.16) is

$$r = A \cos kz + B \sin kz \tag{2.18}$$

where A and B are constants to be determined from the boundary conditions. Matching the slope and ordinate r_0 at $z = S/2$ for a ray which leaves the lens parallel to the axis gives

$$r = r_0 \cos k(z - S/2) \tag{2.19}$$

The 'constant field' strength B_p can be related to the number of turns N and the lens current I using Ampère's circuital law. If the bore of the lens D is sufficiently small that it does not disturb the magnetic circuit and the reluctance of the iron is considered negligible compared to that of the gap S, then we have, for the circuit indicated in Fig. 2.8,

$$B_p = \frac{\mu_0 N I}{S} = 4\pi \times 10^{-7} \left(\frac{NI}{S}\right) \tag{2.20}$$

with I in amperes and B_p in Tesla. Note that B_p gives the flux density in any lens gap if measured sufficiently far from the optic axis.

2.5 Projector lenses

Lenses which use the image formed by a preceding lens as object, such as lenses L2, L3, and L4 of Fig. 2.3, are known as projector lenses. 'Intermediate' lenses fall in this category, to distinguish them from lenses which use a physical specimen as object.

It may happen that the image formed by, say, L2 falls within the lens field of L3. The image formed by L3 can nevertheless be found by the constructions of Section 2.2 if a virtual object is used for L3. This virtual object is the image formed by L2 with L3 removed. A similar procedure applies if the L2 image falls beyond the centre of L3.

The behaviour of real electron trajectories within the lens is given on a simple model by eqn (2.19). This equation is now used to give the focal length and principal plane position of an equivalent ideal lens. The image formed by a system of lenses can then be found by successive applications of the ideal lens construction.

The projector object focus f_p may fall inside or outside the lens field. The two cases are indicated in Figs 2.10(a) and (b). Notice that the extension of the asymptotic ray direction has been used for $z \to -\infty$ to define the 'virtual' or asymptotic projector focal length f_p. The distance between the principal plane H1 and the object-focus in Fig. 2.10(a) is

$$f_p = r_0/\tan\theta = r_0 \Big/ \left(\frac{dr}{dz}\right)_{-\infty} = r_0 \Big/ \left(\frac{dr}{dz}\right)_{-S/2}$$

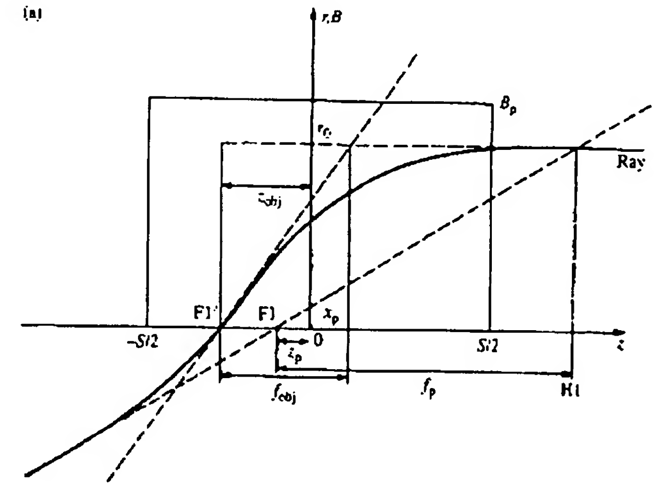

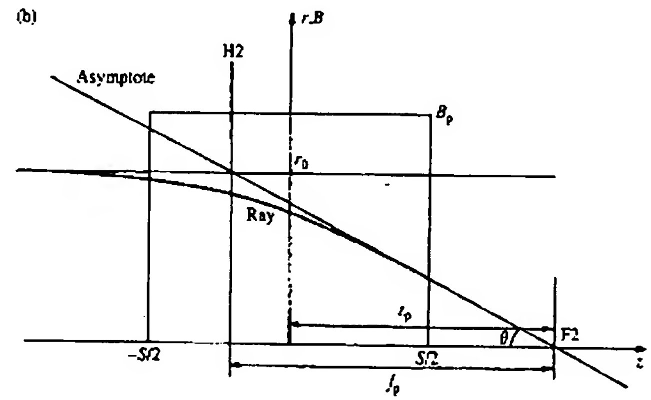

Fig. 2.10 (a) Definition of the objective and projector focal lengths f_{obj} and f_p. The objective and projector focal distances z_{obj} and z_p are also shown. The specimen for an objective lens is placed near F1'. This diagram shows the lens used both as an objective (with focus at F1') and as a projector (with focus F1) if the focus lies inside the lens field. (b) Ray diagram for a projector lens if the focus lies outside the lens field, which extends from $-S/2$ to $S/2$. The ordinate represents both the field strength and the distance of a ray from the optic axis. The image focus occurs at F2.

Using eqn (2.19) gives

$$f_p/S = [Sk \sin(Sk)]^{-1} \tag{2.21}$$

This function is plotted in Fig. 2.11, and shows the minimum focal length characteristic of projector lenses. Lenses are generally operated in the region $0 < Sk < 2$,

Fejes, P. L. (1973). Approximations for the calculation of high resolution electron microscope images of thin films. *Acta Crystallogr.* **A33**, 109.

Fukushima, K., Kawakatsu, H., and Fukami, A. (1974). Fresnel fringes in electron microscope images. *J. Phys. D.* 7, 257.

Goodman, J. W. (1996). *Introduction to Fourier optics*. McGraw-Hill, New York.

Hanszen, K. J. (1971). The optical transfer theory of the electron microscope: fundamental principles and applications. *Adv. Opt. Electron Microsc.* **4**, 1.

Hawkes, P. (1972). *Electron optics and electron microscopy*. Taylor and Francis, London.

Komrska, J. and Lenc, M. (1972). Wave mechanical approach to magnetic lenses. In *Proc. 5th Eur. Congress. Electron Microsc.*, p. 78. Institute of Physics, Bristol.

Lenz, F. (1965). The influence of lens imperfections on image formation. *Lab. Invest.* **14**, 70.

Lynch, D. F., Moodie, A. F., and O'Keefe, M. (1975). N-beam lattice images. V. The use of the charge density approximation in the interpretation of lattice images. *Acta Crystallogr.* **A31**, 300.

Misell, D. L. (1973). Image formation in the electron microscope with particular reference to the defects in electron-optical images. *Adv. Electron. Electron Phys.* 32, 63.

Moodie, A. F. (1972). Reciprocity and shape functions in multiple scattering diagrams. *Z. Naturforsch.* **27a**, 437.

O'Keefe, M. A., Hetherington, C. J. D., Wang, Y. C., Nelson, E. C., Turner, J. H., Kisielowski, C., Malm, J.-O., Mueller, R., Ringnalda, J., Pan, M., and Thust, A. (2001). Sub-Angstrom HREM at 300 keV. *Ultramicroscopy* 89, 215.

Overwijk, M. H. F., Bleeker, A. J., and Thust, A. (1997). Three-fold astigmatism in HREM. *Ultramicroscopy* **67**, 163.

Spence, J. C. H., O'Keefe, M. A., and Kolar, H. (1977). High resolution image interpretation in crystalline germanium. *Optik* **49**, 307.

Wade, R. H. and Frank, J. (1977). Electron microscope transfer functions for partially coherent axial illumination. *Optik* **49**, 81.

Welford, W. T. (1974). *Aberrations of the symmetrical optical system*. Academic Press, London.

Wilson, A. R., Spargo, A. E. C., and Smith, D. J. (1982). The characterisation of instrumental parameters in the high resolution electron microscope. *Optik* 61, 63.

Bibliography

Two excellent texts on imaging theory which emphasize ideas important for high-resolution electron microscopy are:

Martin, L. C. (1966). *The Theory of the microscope*. American Elsevier/Blackie, London.

Goodman, J. W. (1996). *Introduction to Fourier optics*. McGraw-Hill, New York.

Sections of J. M. Cowley's book referenced above also deal with the material of this chapter. Treatments of Fourier electron optics can be found in the articles by Lenz, Hanszen, and Misell cited above.

4

COHERENCE AND FOURIER OPTICS

The coherence of a wavefield refers to its ability to produce interference effects. The high-resolution detail in an electron micrograph arises from coherent interference. In a bright-field image, for example, it is the interference between the central beam and the various waves scattered by the specimen which forms the image. So long as the resolution of the electron microscope was limited by electronic and mechanical instabilities to distances much larger than that coherently illuminated, the question of coherence remained unimportant. These incoherent instabilities no longer limit the resolution of modern electron microscopes and wave-optical interference controls the fine structure of a modern electron image.

Some of the important ideas of optical coherence theory are described below. This theory was developed in optics, but much of it has been found useful in electron optics and the validity of a fundamental optical coherence theorem (the van Cittert–Zernike theorem) has now been tested experimentally for electrons (Burge *et al.* 1975). In optics, the waves emanating from different atomic oscillators in a light source are treated as incoherent. The total intensity in the interference patterns due to each atomic oscillator must be added together. Similarly, the wavefields of successive fast electrons emitted from the filament in the electron microscope are incoherent. In the words of Paul Dirac 'each electron interferes only with itself'. Now the image theory outlined in Chapter 3 was developed for a specimen illuminated by an idealized infinite electron wavetrain. Where many electrons, arriving from slightly different directions, are used to illuminate the specimen the image intensities due to each fast electron must be added together.

Some further qualitative ideas, described in more mathematical detail in the sections which follow, are set out below.

1. An effective source can be defined for an electron microscope. It lies in the exit pupil of the second condenser lens which is usually taken as coincident with the illuminating aperture. The effective source is an imaginary electron emitter filling the illuminating aperture. A mathematical definition is given in Hopkins (1957). Each point within the aperture is supposed to represent a point source of electrons. The emerging spherical wave is approximately plane at the specimen and this is focused to a point in the lens back-focal plane (Fig. 4.1). At the specimen, each electron can be specified by the direction of an incident plane wave. Increasing the size of the illuminating aperture increases the size of the central diffraction spot accordingly. The conditions under which the illuminating aperture may not be incoherently filled are discussed in Section 4.5, in which case this model does not apply.

2. A second important concept is that of spatial coherence width, also known as lateral or transverse coherence width. The term coherence length should be reserved for temporal or longitudinal coherence. The coherence width is the distance at the object over which the illuminating radiation may be treated as perfectly coherent. Thus the scattered waves from a specimen consisting of two atoms separated by less than this distance X_c will interfere and it is the complex amplitudes of these waves which must be added, in this case to produce a cosine-modulated atomic scattering factor. Atoms separated by distances much greater than X_c scatter incoherently and the intensities of their scattered radiation must be added. The intermediate range is described by the theory of partial coherence (see Fig. 4.2).

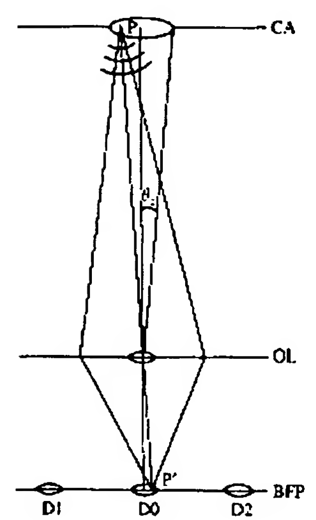

Fig. 4.1 Formation of the central 'unscattered' diffraction spot in an electron microscope. Each point P in the illuminating aperture CA is focused to a point P' in the central diffraction spot DO in the back-focal plane BFP of the objective lens OL. D1 and D2 are two other Bragg reflections. The beam divergence θ_c is also shown.

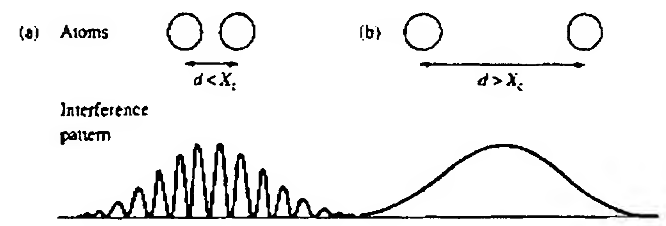

Fig. 4.2 The intensity of scattering recorded at a large distance from two atoms separated by (a) less than the coherence width X_c and (b) a distance much greater than X_c. There is no interference in the second case. The unscattered beam is not shown.

Under normal operating conditions there is a simple relationship between the coherence width X_c and the semi-angle θ_c subtended by the illuminating aperture at the specimen (the beam divergence). This result is given in Section 4.3 as

$$X_c = \lambda/2\pi\theta_c$$

The objective lens pre-field must also be considered (see Section 2.9).

3. The effect of coherence width or beam divergence on the contrast of phase-contrast images is discussed in Section 4.2. This is an important question since it enables the experimentalist to make the best choice of illuminating aperture size for a particular experiment. A strong phase object (one which shows only refractive index variation) produces little contrast unless coherent illumination is used. At the other extreme, source coherence becomes unimportant for the contrast of thick 'amorphous' specimens (such as thick biological specimens) since the phase relationship between scattered waves soon becomes indeterminate with increasing multiple scattering. An approach to the difficult problem of determining the effect of an almost randomly distributed set of atoms on the coherence of a plane wave is described in Sellar (1976). In the intermediate region the contrast of specimens of moderate thickness may be due to interference effects (phase contrast) at high resolution, but incoherent for the coarser image detail. The division between these two ranges of image detail is specified very approximately by the coherence width. Fresnel diffraction, lattice fringes, and single-atom images are three examples of high-resolution phase-contrast detail. To obtain this type of contrast a choice of θ_c must be made which keeps X_c larger than the coarsest detail of interest. Only a range of specimen detail smaller than X_c will produce phase contrast of the type described in Chapter 3 which can be enhanced by the Scherzer optimum focus technique, since this relies on Fresnel interference.

4.1 Independent electrons and computed images

The elastic scattering of a fast electron by a thin specimen is generally treated as two-body problem in which the specimen is described by a suitable complex optical

potential and a solution is obtained for the wavefunction $\psi_0(\mathbf{r}_0, \mathbf{k}_i)$ of the fast electron (incident wavevector $\mathbf{k}_i$) on the specimen exit face. Successive fast electrons are assumed independent and any interaction between them (such as the Boersch effect) is neglected. We assign a separate wavevector and direction to each incident electron. Two electrons with the same wavevector would arrive at the specimen at different times. For an extended source, the intensity at a point in the final image $I(\mathbf{r}_i)$ can be obtained by summing the intensities of the images due to each fast electron. Thus

$$I(\mathbf{r}_i) = \int_{-\infty}^{\infty}\int_{-\infty}^{\infty} |\psi_i(\mathbf{r}_i, \Delta f, \mathbf{K}_0)|^2 F(\mathbf{K}_0) B(\Delta f)\,\mathrm{d}\mathbf{K}_0\,\mathrm{d}\Delta f \qquad (4.1)$$

where $\mathbf{r}$ and $\mathbf{K}_0$ are two-dimensional vectors ($\mathbf{K}_0 = u\hat{\mathbf{i}} + v\hat{\mathbf{j}}$) and $F(\mathbf{K}_0)$ describes the normalized distribution of electron wavevectors. Thus $F(\mathbf{K}_0)\,\mathrm{d}\mathbf{K}_0$ is the probability that the incident electron has a wavevector with $\hat{\mathbf{i}}$ and $\hat{\mathbf{j}}$ components in the range $\mathbf{K}_0$ to $\mathbf{K}_0 + \mathrm{d}\mathbf{K}_0$. Here $\mathbf{k}_i = \mathbf{K}_0 + w\hat{\mathbf{k}}$ and $|\mathbf{k}_i| = 1/\lambda$, with $\hat{\mathbf{i}}, \hat{\mathbf{j}}$, and $\hat{\mathbf{k}}$ orthogonal unit vectors. $B(\Delta f)$ describes the distribution of energy present in the electron beam, and may also include effects due to fluctuations in the objective lens current. All these effects can be represented as time-dependent variations in the focus setting Δf.

It is shown in a later section (and can be demonstrated experimentally using an electron biprism) that to a good approximation the filled final illuminating aperture can be treated as a perfectly incoherent source of electrons. It is thus not necessary to trace each electron back to its source at the filament in using eqn (4.1). For practical computations, the illuminating cone of radiation under focused illumination may be taken as uniformly filled, corresponding to the choice of a 'top-hat' function for $F(\mathbf{K}_0)$ with $|\mathbf{K}_0|_{\max} = |\mathbf{k}_i| \sin\theta_c$, where θ_c is the beam divergence. The exact profile of $F(\mathbf{K}_0)$ can be measured from a densitometer trace taken across the central diffraction spot. A slow emulsion must be used to avoid film saturation.

There are now three possible approaches to the problem of understanding and simulating partial coherence effects in HREM.

1. The images may be computed exactly, using eqn (4.1) and the result of a multiple-scattering computer calculation for $|\psi_i(\mathbf{r}_i, \mathbf{K})|^2$ (see Chapter 5). This method makes no approximation but requires a separate dynamical calculation for each component wavevector $\mathbf{K}_0$ in the incident cone of illumination. The results of such calculations can be found in O'Keefe and Sanders (1975) (see Fig. 4.9).
2. To avoid the need for many dynamical calculations, an approximation valid for small beam divergence may be adopted. This requires a single dynamical calculation for $\psi_i(\mathbf{r}_i, \mathbf{K}_0)$, and is described in Section 5.8.
3. In addition to assuming small θ_c, we may make the further weak-phase object approximation, in order to obtain a result in the form of a multiplicative transfer function. This is done below.

Under rather unusual experimental conditions (see Section 4.5) it may happen that the illuminating aperture is coherently filled. Then the complex image amplitudes for

each incident direction must be summed, rather than their intensities. This occurs if a field-emission electron source is used for HREM work. The appropriate transfer function for this case has been derived by Humphreys and Spence (1981) and O'Keefe and Saxton (1983), and compared with the incoherent illumination case.

4.2 Coherent and incoherent images and the damping envelopes

The labour of detailed image simulation can be avoided and a simple understanding of the effect of coherence on contrast can be obtained for specimens sufficiently thin that the approximation

$$\psi_0(\mathbf{r}_0, \mathbf{K}_0) = \psi_0(\mathbf{r}_0, 0)\exp(2\pi i \mathbf{K}_0, \mathbf{r}_0) \qquad (4.2)$$

can be made. This approximation is satisfied for both the strong- and weak-phase object. Here $\psi_0(\mathbf{r}_0, 0)$ is the specimen exit-face wave for normally incident illumination. The approximation neglects the orientation dependence of scattering within the specimen, that is the rotation of the Ewald sphere with respect to the crystal lattice. The neglect of excitation error effects is equivalent to the neglect of Fresnel diffraction (describing Huygens wavelets) within the specimen if refractive index and propagation effects are taken as separable (see Section 6.3).

For specimens sufficiently thin that eqn (4.2) applies ($t < 5$ nm for low atomic number amorphous specimens), we now consider the two extremes of spatially coherent and incoherent illumination. For the present we ignore chromatic aberration effects and take $B(\Delta f) = \delta(\Delta f)$. The transfer equation for imaging is (Section 3.2)

$$\psi_i(\mathbf{r}_i, \mathbf{K}_0) = \int \psi_0(\mathbf{r}_0, \mathbf{K}_0)\tilde{A}(\mathbf{r}_i - \mathbf{r}_0)\,\mathrm{d}\mathbf{r}_0 \qquad (4.3)$$

Using eqns (4.1), (4.2), and (4.3) gives

$$I(\mathbf{r}_i) = \int\int \psi_0(\mathbf{r}_0, 0)\psi_0^*(\mathbf{r}_0', 0)\tilde{A}(\mathbf{r}_i - \mathbf{r}_0)\tilde{A}^*(\mathbf{r}_i - \mathbf{r}_0')\gamma(\mathbf{r}_0' + \mathbf{r}_0)\,\mathrm{d}\mathbf{r}_0\,\mathrm{d}\mathbf{r}_0' \qquad (4.4)$$

where

$$\gamma(\mathbf{r}_0) = \int F(\mathbf{K}_0)\exp(-\pi i \mathbf{K}_0 \cdot \mathbf{r}_0)\,\mathrm{d}\mathbf{k} \qquad (4.5)$$

The function $\gamma(\mathbf{r}_0)$, if normalized, is known as the complex degree of coherence as will be discussed in Section 4.3.

For coherent illumination, $F(\mathbf{K}_0) = \delta(\mathbf{K}_0)$ and $\gamma(\mathbf{r}_0) = 1$, so that eqn (4.4) becomes

$$I(\mathbf{r}_i) = \left|\int \psi_0(\mathbf{r}_0, 0)\tilde{A}(\mathbf{r}_i - \mathbf{r}_0)\,\mathrm{d}\mathbf{r}_0\right|^2 \qquad (4.6)$$

in agreement with the image intensity given by eqn (4.3) for normal plane-wave illumination. For perfectly incoherent illumination, $F(\mathbf{K}_0)$ is constant and $\gamma(\mathbf{r}_0) = \delta(\mathbf{r}_0)$

and we obtain

$$I(\mathbf{r}_i) = \int |\psi_0(\mathbf{r}_0, 0)|^2 |\hat{A}(\mathbf{r}_i - \mathbf{r}_0)|^2 \, d\mathbf{r}_0 \qquad (4.7)$$

For a pure-phase object, as discussed in Section 1.1 and used as a model for ultra-thin biological specimens, we have

$$\psi_0(\mathbf{r}_0, 0) = \exp(-i\sigma\phi_p(\mathbf{r}_0))$$

where $\phi_p(\mathbf{r})$ is real. Since the squared modulus of this function is unity, eqn (4.7) indicates that no contrast is possible from such a specimen using perfectly incoherent illumination (see also Section 1.2). In practice one is always dealing with partially coherent illumination, since a perfectly incoherent imaging system would require an illumination aperture of infinite diameter.

Loosely speaking then, using a very small condenser aperture in the electron microscope is rather like using a laser source in optics, while a large aperture corresponds to a tungsten lamp source.

For specimens satisfying eqn (4.2) the transfer of information in the electron microscope is thus linear in complex amplitude under coherent illumination and linear in intensity under incoherent illumination.

We now consider the important intermediate case of partial coherence with which microscopists are chiefly concerned in practice. The incorporation of the effects of partial spatial and temporal coherence into the transfer function described earlier (eqn 3.24) has been described by many workers. Results for an incoherently filled disc-shaped effective source have been briefly described in Section 3.3 (see also Appendix 3). We will rely mainly on the works of Frank (1973) and Fejes (1977) which gives a useful estimate of the effects of partial coherence on images for the simpler case of a Gaussian distribution of intensity across the effective source. For small effective source widths and a central zero-order diffracted beam much stronger than any other, these workers have shown that the combined effects of partial coherence and electronic instabilities lead to a transfer function of the form

$$\begin{aligned} A(\mathbf{K}) &= P(\mathbf{K}) \exp[i\chi(\mathbf{K})] \exp\{-\pi^2\Delta^2\lambda^2\mathbf{K}^4/2\} \gamma(\nabla\chi/2\pi) \\ &= P(\mathbf{K}) \exp[i\chi(\mathbf{K})] \exp\{-\pi^2\Delta^2\lambda^2\mathbf{K}^4/2\} \exp\{-\pi^2 u_0^2 \mathbf{q}\} \qquad (4.8a) \end{aligned}$$

in the absence of astigmatism. As discussed earlier in Sections 3.3 and 2.8.2, the quantities $\chi(\mathbf{K})$ and Δ are defined by

$$\chi(\mathbf{K}) = \pi\Delta f \lambda \mathbf{K}^2 + \pi C_s \lambda^3 \mathbf{K}^4/2 \qquad (4.8b)$$

with $\mathbf{K}$ the vector $u\hat{\mathbf{i}} + v\hat{\mathbf{j}}$ where $(u^2 + v^2)^{1/2} = |\mathbf{K}| = \theta/\lambda$, and

$$\Delta = C_c Q = C_c \left[\frac{\sigma^2(V_0)}{V_0^2} + \frac{4\sigma^2(I)}{I_0^2} + \frac{\sigma^2(E_0)}{E_0^2} \right]^{1/2} \qquad (4.9)$$

where $\sigma^2(V_0)$ and $\sigma^2(I)$ are the variances in the statistically independent fluctuations of accelerating voltage V_0 and objective lens current I_0 respectively. (Evidence for correlated fluctuations has recently appeared.) The root-mean-square value of the high-voltage fluctuation is thus equal to the standard deviation $\sigma(V_0) = [\sigma^2(V_0)]^{1/2}$. A term has also been added to account for the energy distribution of electrons leaving the filament. The full width at half the maximum height of the energy distribution of electrons leaving the filament is

$$\Delta E = 2.345\sigma(E_0) = 2.345[\sigma^2(E_0)]^{1/2}$$

The normalized Gaussian distribution of intensity assumed for the incoherent effective electron source has the form

$$F(\mathbf{K}_0) = \left(\frac{1}{\pi u_0^2}\right) \exp\left(-\frac{\mathbf{K}_0^2}{u_0^2}\right)$$

If the beam divergence is chosen as the angular half-width θ_c for which this distribution falls to half its maximum value, then u_0 is defined by

$$\theta_c = \lambda u_0 (\ln 2)^{1/2}$$

The quantity $\mathbf{q}$ in eqn (4.8a) is

$$\mathbf{q} = (C_s\lambda^3\mathbf{K}^3 + \Delta f \lambda \mathbf{K})^2 + (\pi^2\lambda^4\Delta^4\mathbf{K}^6 - 2\pi^4 i \lambda^3 \Delta^2 \mathbf{K}^3) \qquad (4.10)$$

A clear understanding of the properties of eqn (4.8) is essential for the microscopist seriously interested in ultra-high-resolution work, since it expresses all the resolution-limiting factors of practical importance (except specimen movement). The relative importance of these factors is discussed in more detail in Appendix 3. For the present, we note the following features of eqn (4.8).

1. A crucial approximation is the assumption of a strong zero-order diffracted beam. This condition is satisfied both in very thin crystals and in thicker areas of wedge-shaped crystals showing crystals showing strong Pendellösung, as described in Section 5.6. Note that terms such as those containing $\Phi_{\mathbf{h}}\Phi_{-\mathbf{h}}$ in eqn (5.9) which lead to the appearance of 'half-period fringes' are neglected in this analysis. These fringes have been used in the past to give a misleading impression of high-resolution detail (see Section 10.10).

2. The last bracketed complex term in eqn (4.10) expresses a coupling between the effects of using a finite incident beam divergence angle θ_c (partial spatial coherence) and the consequences of using a non-monochromatic electron beam (partial temporal coherence, $\Delta \neq 0$). The magnitude of this coupling term has been investigated in detail by Wade and Frank (1977), who find that, under high-resolution conditions (e.g. $\theta_c < 0.001$ rad, $\Delta < 20$ nm at 100 kV—their paper should be consulted for other conditions) this term can frequently be neglected. Then eqn (4.8) contains three

multiplicative factors, each of which imposes a resolution limit by attenuating high-order spatial frequencies. The first term $P(\mathbf{K})$ expresses the diffraction limit imposed by the objective aperture. The third term describes a damping envelope more severe than Gaussian attenuation with a width

$$u_0(\Delta) = [2/(\pi\lambda\Delta)]^{1/2} \tag{4.11}$$

which will *always* be present even if the objective aperture is removed. This resolution limit $d \approx 1/u_0(\Delta)$ is independent of the illumination conditions used and depends on the existence of instabilities in the objective lens and high-voltage supplies and on the thermal spread of electron energies. The last term in eqn (4.8) shows an apparently complicated dependence on illumination semi-angle θ_c, focus Δf, spherical aberration constant C_s, and wavelength λ. Its behaviour can be given a simple interpretation, however, since the function $\gamma(\nabla\chi/2\pi)$ is just the Fourier transform of the source intensity distribution evaluated with the function's argument equal to the local slope of the aberration function $\chi(\mathbf{K})$. For a Gaussian source, $\gamma(\mathbf{K})$ is also Gaussian and has a width which is inversely proportional to the width of the source. Thus $\gamma(\nabla\chi/2\pi)$ is small in regions where the slope of $\chi(\mathbf{K})$ is large, resulting in severe attenuation of these spatial frequencies. Conversely, in the neighbourhood of regions where the slope of $\chi(\mathbf{K})$ is small, all spatial frequencies are well transmitted by the microscope with high contrast.

Extended regions over which the slope of $\chi(\mathbf{K})$ is small are called passbands or contrast transfer intervals and these can be found for many focus settings, given by

$$\Delta f_n = [C_s\lambda(8n+3)/2]^{1/2} \tag{4.12}$$

This result may be obtained as follows. By differentiation, it is easily shown that the slope of $\chi(\mathbf{K})$ is zero at K_1 for the corresponding 'stationary phase' focus $\Delta f_0 = -C_s\lambda^2K_1^2$ (see Fig. A3.1). We require that K_1, lie at the centre of the passband, in order to minimize the damping effects of limited spatial coherence. As a separate condition, however, we also require $\chi = n\pi/2$, with $n = -1, -5-9, -13$, etc., for good phase contrast (see Section 3.4). Then both the scattering phase shift $\exp(-i\pi/2) = -i$ in eqn (3.26) and the lens phase shift $\exp(-i\pi/2)$ (see eqn 3.27b) have the same sign, as needed to obtain a high-contrast image which is darker in regions of high potential. We might therefore impose the additional condition that

$$\chi(\Delta f_0) = -\frac{\pi}{2}(1, 5, 9, 13, \ldots)$$

in order to select only negative maxima in $\sin\chi$ for the centre of the passband. However, the passband can be made broader if the value of $\sin\chi(K_1)$ is allowed to decrease slightly as shown by the dip in the passband of Fig. 4.3(b). This is achieved

by taking

$$\chi(\Delta f_0) = -\frac{\pi}{2}\left(\frac{8n+3}{2}\right) = -\pi C_s\lambda^3K^4/2$$

Solving this for K and using this value for K_1 in the stationary phase focus expression gives eqn (4.12). This procedure guarantees both that the slope of $\chi(\mathbf{K})$ is zero (as sketched in Fig. A3.1) and that $\sin\chi = -1$ in the middle of the passband. The zero-order passband ($n = 0$) is commonly known as the 'Scherzer focus' and is the optimum choice of focus for images of defects or single molecules for which a straightforward interpretation in terms of object structure is required (see Section 6.2). Some examples of these passbands are shown in Fig. 4.3. They are seen to move out toward higher spatial frequencies with increasing n and, as discussed in Appendix 3 in more detail, to become narrower with increasing n and C_s. Once the slope of $\chi(\mathbf{K})$ exceeds a certain value beyond these passbands, all spatial frequencies are severely attenuated. This attenuation is the major consequence of using a cone of illumination to illuminate the specimen from an extended incoherent source. By collecting several images at, say, the $n = 0, 1, 2, 3$ focus values specified by eqn (4.12) and processing these by computer, a composite image can be built up using only the well-transmitted spatial frequencies within the passband from each image, and this idea is the basis of image-processing schemes discussed in Chapter 7. These passbands cannot, however, be moved out beyond the resolution limit set by electronic instabilities (eqn 4.11). Figure 4.3 shows the transfer function drawn out for a typical instrument with $C_s = 2.2$ mm, $\Delta = 120$ Å, $\theta_c = 0.9$ mrad at an operating voltage of 100 kV. To a good approximation the functions shown can be taken to be the last two terms of eqn (4.8) multiplied by $\sin\chi(|\mathbf{K}|)$ with the second, bracketed term in eqn (4.10) set equal to zero (see Appendix 3).

There are, therefore, two resolution limits which can be quoted for an electron microscope. The first, generally called the point-resolution of the instrument, is set by the first zero crossing of the transfer function at the Scherzer focus ($n = 0$ in eqn 4.12). This is the useful resolution limit of the instrument for the analysis of defects and other non-periodic specimens. On high-voltage machines, the stability-resolution limit (eqn 4.11) may occur at a lower spatial frequency than the Scherzer cut-off (see eqn 6.17), in which case eqn (4.11) would determine the point-resolution of the machine (see Appendix 3).

The second resolution specification for an instrument might be called the information-resolution limit. It is set by electronic instabilities and given by eqn (4.11). For 100 kV machines this resolution limit generously exceeds the point-resolution, which is chiefly limited by spherical aberration. The information-resolution limit expresses the highest-resolution detail which could be extracted from a micrograph by the methods of image processing (leaving aside problems of electron noise) and can be measured by the Young's fringe diffractogram technique of Frank (see Section 10.7) or by finding the finest three-beam lattice fringes from a perfect crystal which the instrument is capable of recording under axial, *kinematic* conditions (but

ATTACHMENT A
Ser. No.: 10/656,342
Page 16

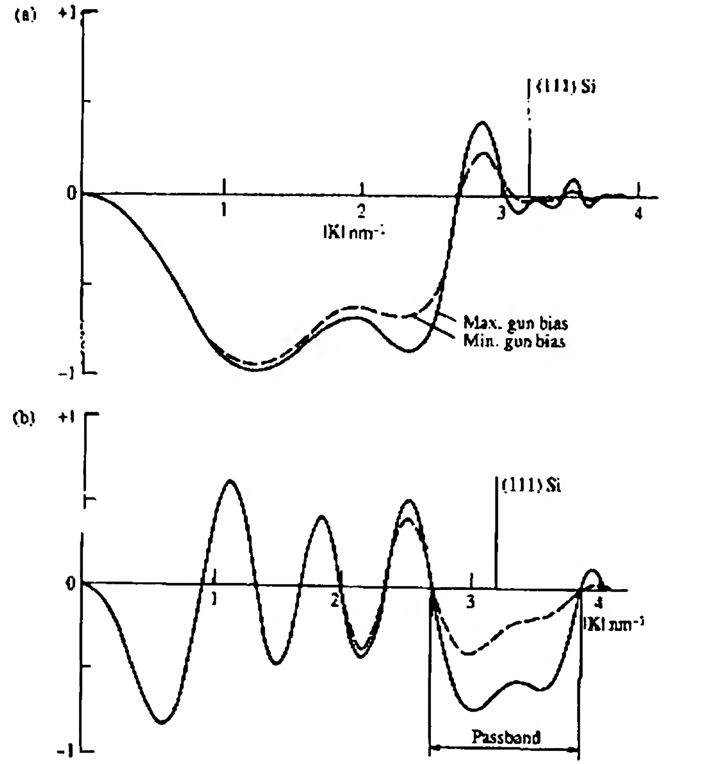

Fig. 4.3 Transfer functions for a 100 kV electron microscope with C_s = 2.2 mm and beam divergence θ_c = 0.9 mrad. The cases $n = 0$ (Scherzer focus, $\Delta f = -110.4$ nm) and $n = 3$ ($\Delta f = -331.5$ nm) of eqn (4.12) are shown in (a) and (b) respectively. In (a) the 'passband' extends from $u = 0$ out to the point-resolution limit of the instrument, in (b) the passband has moved out to the position indicated. The solid curves are drawn for maximum gun-bias setting (Δ = 5.4 nm) and the dotted curves show the effect of using the minimum gun-bias setting (maximum beam current Δ = 12.0 nm) resulting in increased attenuation of the higher spatial frequencies. Note that the value of n is equal to the number of minima which precede the passband. The position of the (111) Bragg reflection is indicated and is seen to fall beyond the point-resolution limit (see Section 5.8). The imaginary part of eqn (4.8) has been plotted.

see Section 5.8). If there is no diffuse scattering between the Bragg reflections, a focus setting can then be found which places one of the passbands of eqn (4.11) across the Bragg reflection of interest. Defects and non-periodic detail in such an image cannot usually be simply interpreted (see Sections 5.8 and 10.10).

The availability of gun monochromators for HREM machines now allows a reduction of ΔE, at the cost of image intensity. If the other electronic instabilities in eqn (4.9) allow it, this may improve the image quality, as described in den Dekker *et al.* (2001).

4.3 The characterization of coherence

The extent to which the wavefield at neighbouring points on the object vibrates in unison is expressed naturally by the correlation between wave amplitudes at points $\mathbf{r}_1$ and $\mathbf{r}_2$ and is given by the cross-correlation function

$$\Gamma(|\mathbf{r}_1 - \mathbf{r}_2|, T) = \lim_{\tau\to\infty} \int_{-\tau}^{\tau} \psi^*(\mathbf{r}_1, t)\psi(\mathbf{r}_2, t - T)\, dt \qquad (4.13)$$

A spatially stationary field has been assumed. When normalized, this function is called the complex degree of coherence $\gamma(x_{1,2}, T)$. Here $x_{1,2} = |\mathbf{r}_1 - \mathbf{r}_2|$. The function contains a spatial dependence expressing lateral or transverse coherence and a time dependence expressing temporal or longitudinal coherence. In electron microscopy, the temporal coherence is large and we are chiefly concerned with $\gamma(x_{1,2}, 0) = \gamma(x_{1,2})$. In order to obtain strong interference effects such as Bragg scattering from adjacent scattering centres we require the wavefield at these points to be well correlated. That is, that $\gamma(x_{1,2})$ is large for this value of $x_{1,2}$.

The van Cittert–Zernike theorem relates $\gamma(x_{1,2})$ through a Fourier transform to the function $F(k)$ used in Sections 4.1 and 4.2. Despite differences in the nature of the particles (photons are bosons, electrons are fermions) and differing interpretations of the wavefunction, the results of electron interference experiments suggest that this important optical theorem may be taken over into electron optics. It will be seen that the range of object spacings which can be considered coherently illuminated is proportional to the width of $\gamma(x_{1,2})$, so that a narrow source (for which $\gamma(x_{1,2})$ is a broad function) produces more coherent radiation than does a larger source. The theorem only applies to perfectly incoherent sources.

While the effects of partial coherence are important for images, they are seen most dramatically in interference experiments. A familiar example of a near-field interference experiment is the observation of Fresnel fringes at an edge, as discussed in Chapter 10. Note that questions of partial coherence only arise when more than one idealized point source of radiation is used. An interference experiment which may be used to measure $\gamma(x_{1,2})$ is Young's slit experiment. This experiment gives an important physical interpretation to $\gamma(x_{1,2})$—it is the contrast of the interference fringes (if the pin-holes are sufficiently small). Figure 4.4 shows the experimental arrangement used in optics. The relationship between the fringe contrast and the source size is described in most optics texts (e.g. Born and Wolf 1975). Sharp fringes are obtained from a single point-source P_1. Moving this source to P_2 translates the fringes in the opposite direction. The incoherent superposition of many sets of fringes, slightly out of register and arising from a set of sources along P_1P_2 results in a fringe pattern of reduced contrast. An important point is that a small increase in the width of the source will have more effect on the contrast of fine fringes than on coarse fringes. A similar result holds for the effect of source size (condenser aperture) on high-resolution phase-contrast images.

Figure 4.5 shows the result of performing Young's slit experiment with electrons. If the pin-holes are sufficiently small in the optical case, the Michelson visibility

Spatial Coherence Characterization of Undulator Radiation

C. Chang*, P. Naulleau, E. Anderson and D. Attwood*
Center for X-Ray Optics, Lawrence Berkeley Laboratory, Berkeley, CA 94720, USA
**Department of EECS, University of California, Berkeley, CA 94720, USA*

Introduction

Coherent radiation offers important opportunities for both science and technology. The well defined phase relationships characteristic of coherent radiation, allow for diffraction-limited focusing (as in scanning microscopy), set angular limits on diffraction (as in protein crystallography), and enable the convenient recording of interference patterns (as in interferometry and holography[1,2]). While coherent radiation has been readily available and widely utilized at visible wavelengths for many years, it is just becoming available for wide use at shorter wavelengths[3,4]. This is of great interest as the shorter wavelengths, from the extreme ultraviolet (EUV, 10-20 nm wavelength), soft x-ray (1-10 nm), and x-ray (<1 nm) regions of the spectrum, correspond to photon energies that are well matched to the primary electronic resonances (K-shell, L-shell, etc.) of essentially all elements, thus providing a powerful combination of techniques for the elemental and chemical analysis of physical and biological materials at very high spatial resolution. Tunable, coherent radiation in these spectral regions is available primarily due to the advent of undulator radiation at modern synchrotron facilities, where relativistic electron beams of small cross-section transverse periodic magnet structures, radiating very bright, powerful, and spatially coherent radiation at short wavelengths. Recent progress with EUV lasers, high laser harmonics, and free electron lasers may soon add to these capabilities. In this paper we utilize the classic two-pinhole diffraction technique, an extension of Young's two-slit interference experiment, to simply and accurately characterize the degree of spatial coherence provided by undulator radiation. We show that, with the aid of modest pinhole spatial filtering, undulator radiation can provide tunable short wavelength radiation with a very high degree of spatial coherence at presently available user facilities. Spatially coherent power of order 30 mW is available in the EUV, and is expected to scale linearly with wavelength to about 0.3 mW in the hard x-ray region.

Experiment

For radiation with a high degree of coherence and a well-defined propagation direction, it is convenient to describe coherence properties in longitudinal and transverse directions. For a source of diameter d, emission half-angle θ, and full spectral bandwidth $\Delta\lambda$ at wavelength λ, relationships for full spatial coherence and longitudinal coherence length, l_{coh}, are given respectively by

$$d \cdot \theta = \lambda/2\pi \tag{1}$$

and

$$l_{coh} = \lambda^2/2\Delta\lambda \tag{2}$$

where d, θ, and $\Delta\lambda$ are $1/\sqrt{e}$ measures of Gaussian distributions. Based on measures of the source size and theoretical predictions of the emission angle, it is estimated that undulator radiation, as discussed in this paper, emanating from an electron beam of highly elliptical cross-section, will approach full spatial coherence Eq.(1) in the vertical plane, while being coherent over only a fraction of the radiated beam in the horizontal direction. Here we

present a detailed characterization of an undulator beamline optimized for operation in the EUV regime.

Undulator beamline 12.0 was developed to support high-accuracy wave-front interferometry of EUV optical systems. With an electron beam of elliptical cross-section, having a vertical size $d_v = 2\sigma_v = 32\,\mu m$, and an emission half-angle $\theta = 80\,\mu rad$ (the central radiation cone containing a $1/N$ relative spectral bandwidth), the product $d \cdot \theta$ is just slightly larger (20%) than $\lambda/2\pi$ at the $13.4\,nm$ wavelength used in these experiments. Thus we expect to see strongly correlated fields, of high spatial coherence, in the vertical plane. The horizontal beam size is considerably larger with $d_h = 2\sigma_h = 520\,\mu m$, so that with approximately the same emission half-angle we expect it to be spatially coherent over only a fraction of the horizontal extent of the radiated beam.

The coherence properties of undulator radiation within the central radiation cone have been measured using the well known Thompson-Wolf two-pinhole method[5]. A very high degree of spatial coherence is demonstrated, as expected on the basis of a simple model. The effect of an asymmetric source size on the resultant coherence properties is observed, and is consistent with aperturing within the beamline optical system used to transport radiation to the experimental chamber. Based on these observations and well understood scaling of undulator radiation, it is evident that high average power, spatially coherent radiation is available at modern storage rings with the use of appropriate pinhole spatial filtering techniques.

References

[1] P. Naulleau *et al*, Appl. Optics, **38**, p. 3523, 1999
[2] K. Goldberg, P. Naulleau, & J. Bokor, J. Vac. Sci. Technol. B **17**, 2982 (1999)
[3] D.T. Attwood, K. Halbach and K.-J Kim, Science, **228**, p.1265, 1985
[4] D.T. Attwood *et al*, IEEE J. Quant. Electron., **35**, p. 709, 1999
[5] B. J. Thompson and E. Wolf, J. Opt. Soc. Amer., **47**, 895(1957)

Acknowledgement

The authors would like to thank Dr. Kenneth Goldberg for valuable discussion. Special thanks are due to the entire CXRO engineering team and most notably to Phil Batson, Paul Denham, Drew Kemp and Gideon Jones for bringing the experimental hardware to fruition. This work was supported by the Air Force office of Scientific Research and the DOE office of Basic Energy Sciences.

Principal investigator: David Attwood, Center for X-Ray Optics, LBL. DTAttwood@lbl.gov.

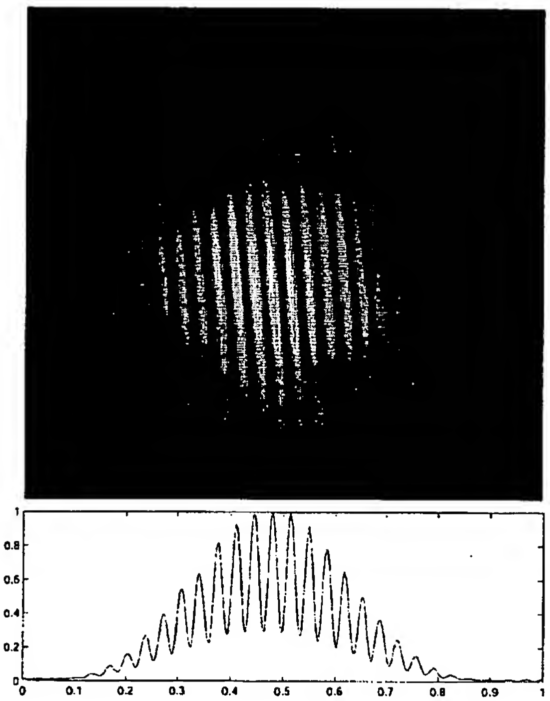

Figure 1: Measured two-pinhole interference patterns for horizontal pinhole separation of 4-μm, with a beamline acceptance aperture of half-angle $48 \mu rad$. Pairs of nominally 450 nm diameter are used. Images are recorded on an EUV CCD camera. The wavelength used is $\lambda = 13.4 nm$ with a bandwidth of $\lambda/\Delta\lambda = 55$. The pinhole diffraction patterns overlap and produce the Airy envelope.

Transmission Electron Microscope (TEM)

TEMs are patterned after Transmission Light Microscopes and will yield similar information.

Morphology

The size, shape and arrangement of the particles which make up the specimen as well as their relationship to each other on the scale of atomic diameters.

Crystallographic Information

The arrangement of atoms in the specimen and their degree of order, detection of atomic-scale defects in areas a few nanometers in diameter

Compositional Information (if so equipped)

The elements and compounds the sample is composed of and their relative ratios, in areas a few nanometers in diameter

---

A TEM works much like a slide projector. A projector shines a beam of light through (transmits) the slide, as the light passes through it is affected by the structures and objects on the slide. These effects result in only certain parts of the light beam being transmitted through certain parts of the slide. This transmitted beam is then projected onto the viewing screen, forming an enlarged image of the slide.

TEMs work the same way except that they shine a beam of electrons (like the light) through the specimen(like the slide). Whatever part is transmitted is projected onto a phosphor screen for the user to see. A more technical explanation of a typical TEMs workings is as follows (refer to the diagram below):

---

1. The "Virtual Source" at the top represents the electron gun, producing a stream of monochromatic electrons.
2. This stream is focused to a small, thin, coherent beam by the use of condenser lenses 1 and 2. The first lens(usually controlled by the "spot size knob") largely determines the "spot size"; the general size range of the final spot that strikes the sample. The second lens(usually controlled by the "intensity or brightness knob" actually changes the size of the spot on the sample; changing it from a wide dispersed spot to a pinpoint beam.
3. The beam is restricted by the condenser aperture

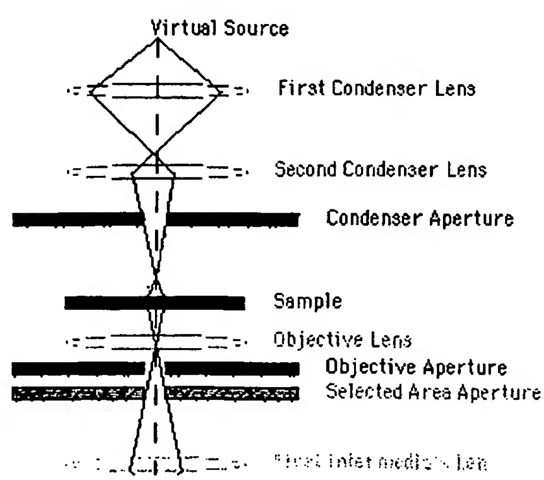

(usually user selectable), knocking out high angle electrons (those far from the optic axis, the dotted line down the center)

4. The beam strikes the specimen and parts of it are transmitted
5. This transmitted portion is focused by the objective lens into an image
6. Optional Objective and Selected Area metal apertures can restrict the beam; the Objective aperture enhancing contrast by blocking out high-angle diffracted electrons, the Selected Area aperture enabling the user to examine the periodic diffraction of electrons by ordered arrangements of atoms in the sample
7. The image is passed down the column through the intermediate and projector lenses, being enlarged all the way
8. The image strikes the phosphor image screen and light is generated, allowing the user to see the image. The darker areas of the image represent those areas of the sample that fewer electrons were transmitted through (they are thicker or denser). The lighter areas of the image represent those areas of the sample that more electrons were transmitted through (they are thinner or less dense)